Electronic Supplementary Information

Thermally activated delayed fluorescent platinum(II) complex for red organic light emitting diodes with high efficiencies and small roll-off

Jian-Gong Yang,† Nengquan Li,† Jiayu Li, Xiu-Fang Song, Ming-De Li, Jingling Zhang and Kai Li**

J.-G Yang, N. Li, X.-F. Song, J. Zhang, K. Li
Shenzhen Key Laboratory of New Information Display and Storage Materials, Guangdong Provincial Key Laboratory of New Energy Materials Service Safety, College of Materials Science and Engineering, Shenzhen University, Shenzhen 518055, P. R. China.

J.-G Yang
Hubei Key Laboratory of Biomass Fibers and Eco-dyeing & Finishing, Department of Chemistry and Chemical Engineering, Wuhan Textile University, Wuhan 430200, P. R. China

J. Li, M.-D. Li
College of Chemistry and Chemical Engineering, Key (Guangdong-Hong Kong Joint) Laboratory for Preparation and Application of Ordered Structural Materials of Guangdong Province, Shantou University, Guangdong 515063, P. R. China

† Jian-Gong Yang and Nengquan Li contributed equally.

Experimental Procedures

Materials

All starting materials were purchased from commercial sources and used as received without further purification unless otherwise indicated. Solvents used for film preparations and photophysical measurements were of HPLC grade. Potassium tetrachloroplatinate(II) and 3,6-di-tert-butyl carbazole were purchased from Energy Chemical. 1,4-phenylenediboronic acid and 2-bromopyridine were purchased from Bide Pharmatech. 3-(3,6-di-tert-butyl-9H-carbazol-1-yl)dibenzo[a,c]phenazine (L1) and 3-(3,6-di-tert-butyl-8-(dibenzo[a,c]phenazin-3-yl)-9H-carbazol-1-yl)-6-(3,6-di-tert-butyl-9H-carbazol-1-yl)dibenzo[a,c]phenazine (L2) were prepared by following literature methods.[1,2]

Instruments and Methods

General methods

^{1}H and ^{13}C Nuclear magnetic resonance (NMR) spectra were acquired using a Bruker Avance 400 and 500 FT-NMR spectrometers at room temperature. Deuterated chloroform was used as the solvent, and tetramethylsilane (TMS) served as the internal reference. Elemental analyses were measured on a Vario Micro cube with CHN mode. High-resolution mass spectrometry (HRMS) was performed on AB SCIEX TripleTOF 6600 (Singapore) and Agilent QTOF 6550. Thermogravimetric analysis (TGA) was conducted on a TGA-Q50 Instrument (TA Instruments, America) with a heating rate of 10 ^{o}C/min from 50 to 800 ^{o}C under nitrogen atmosphere.

UV-vis absorption spectra were obtained on a Shimadzu UV-2600 spectrophotometer (Shimadzu, Japan) at room temperature. Steady-state emission spectra were recorded on a Hitachi F-7100 spectrometer with a xenon lamp as an excitation light source. The transient photoluminescence spectra were measured using a single photon counting spectrometer (Picoquant, FluoTime 300, Germany) with a Picosecond Pulsed UV-LASTER (LASTER375 and 485) as the excitation source. Variable temperature transient photoluminescence measurements were recorded with the aid of an Oxford 2 Instruments continuous flow cryostat. The absolute photoluminescence quantum yields (PLQYs) were measured on a Hamamatsu UV-NIR absolute PL quantum yield spectrometer (C13534, Hamamatsu Photonics) equipped with a calibrated integrating sphere under argon atmosphere. The PMMA (5 wt%) doped film samples were prepared by drop-casting 1,2-dichloroethane solutions.

Cyclic voltammetry (CV) measurements were carried out on a CHI600 electrochemical analyzer (Chenhua, China) at room temperature, with a conventional three-electrode system consisting of a glassy

carbon working electrode, a platinum wire auxiliary electrode, and an Ag/AgCl standard electrode was used as the reference electrode. Dichloromethane and tetrabutylammonium hexafluorophosphate (0.1 M) were used as the solvent and supporting electrolyte, respectively.

Femtosecond transient absorption (fs-TA) experiment was performed based on a femtosecond Ti:Sapphire regenerative amplified Ti:Sapphire laser system (Coherent, Astrella-Tunable-F-1k), femtosecond transient absorption spectrometer system (Ultrafast Systems, Helios Fire) and Femtosecond Up-conversion fluorescence Kinetic Spectrometer (FluoMax-MP). The repetition frequency of amplifier is 1 kHz, the pulse width of 800 nm is 84 fs, and the output power of 800 nm from amplifier is 7.4 W. For fs-TA experiment, the probe pulse is obtained by using approximately 4% of the amplified 800 nm output from the Astrella to generate a white-light continuum (320−700 nm) using a CaF_2 plate. Fiber optics is coupled to a multichannel spectrometer with a CMOS sensor that has a 1.5 nm intrinsic resolution. The maximum extent of the temporal delay was 8 ns. The instrument response function is determined to be ca.120 fs. At each temporal delay, data were averaged for 2 s and collected by the acquisition system. For the experiments described in this study, the sample solutions were excited by 400 nm pump beam (200 μW, from TOPAS). For fs-TRF experiments, 400 nm (200 μW) was used as pump laser and 800 nm (200 μW) was used as gain laser to get the up-conversion signal. The instrument has a time window of 6 ns with sub-100 fs intrinsic time resolution. Spectral resolution in the visible range is 0.7 to 8 nm depends on the wavelength.

Arrhenius plot for the temperature-dependent lifetimes fitting analysis

k_{TADF} values can be fitted to a two-level model using Equation S1.[3,4] The Arrhenius plot shows a linear dependence of ln k_{TADF} as a function of 1/T with a slope of $\Delta E_{ST}/k_B$. The intercept of ln$b$ is collectively determined by the $S_1 \rightarrow T_1$ ISC rate constant (k_{ISC}) and the radiative rate of the singlet excited state (k_{fl}). The radiative rate constant (k_{TADF}) at each temperature was estimated from the emission quantum yield and lifetime.

$$\ln(k_{TADF}) = \ln\left(\frac{k_{ISC}^{S_1}}{3}\left(1 - \frac{k_{ISC}^{S_1}}{k_{fl} + k_{ISC}^{S_1}}\right)\right) - \frac{\Delta E_{S_1-T_1}}{k_B T}$$

$$= \ln b - \frac{\Delta E_{S_1-T_1}}{k_B T} \quad \text{(S1)}$$

Boltzmann type equation for the temperature-dependent lifetimes fitting analysis

Boltzmann type equation is shown in Equation S2[3,5], where $\tau(S_1)$ and $\tau(T_1)$ are the lifetimes for the S_1 and T_1 states, respectively, k_B is Boltzmann's constant, and T is temperature.

$$\tau(T) = \frac{3+exp\left[-\frac{\Delta E(S_1-T_1)}{k_B T}\right]}{\frac{3}{\tau(T_1)}+\frac{1}{\tau(S_1)}exp\left[-\frac{\Delta E(S_1-T_1)}{k_B T}\right]} \quad \text{(S2)}$$

Estimation of the ratio of TADF to direct phosphorescence

With the fluorescence and phosphorescence rates and $\Delta E_{S1\text{-}T1}$ values (taking from Boltzmann analysis), it is possible to estimate the contribution of TADF and direct phosphorescence to the observed emission from a TADF emitter.[6] These equations are given below.

$$\%TADF = \left[1 - \left(1 + \frac{k_{fl}}{3k_{ph}} e^{-\frac{\Delta E_{S1-T1}}{k_B T}}\right)^{-1}\right] \times 100$$

$$\%T_1 Phosphorescence = \left[\left(1 + \frac{k_{fl}}{3k_{ph}} e^{-\frac{\Delta E_{S1-T1}}{k_B T}}\right)^{-1}\right] \times 100 \quad \text{(S3)}$$

The equlibrium constant (K_{eq}) for the $T_1 \rightleftharpoons S_1$

$$K_{\mathrm{eq}} = \frac{k_{\mathrm{RISC}}}{k_{ISC}} = \frac{1}{3} exp\left(-\frac{\Delta E_{S_1-T_1}}{k_{\mathrm{B}} T}\right) \quad \text{(S4)}$$

Single Crystal Analysis

Single crystals suitable for X-ray diffraction analysis were obtained by evaporation of a mixture of dichloromethane and n-hexane solution (v/v = 1:10) over a period of several days. X-ray single-crystal diffraction data of the compounds were recorded on a Bruker D8 Venture diffractometer using Cu Kα radiation (λ = 1.54178 Å). The crystals were kept at 100.0 and 298 K during data collection. Using Olex2,[7] the structure was determined with the ShelXT[8] structure solution program using intrinsic phasing and refined with the ShelXL refinement package using least-squares minimization.[9] Full crystallographic information in CIF format has been deposited at the Cambridge Crystallographic Data Center (CCDC) under deposition number 2205684 and 2205685 for **Pt1** and **Pt2**, respectively.

Device Fabrication and Measurement

The OLEDs have a structure of ITO/HAT-CN (5 nm)/TAPC (30 nm)/TCTA (15 nm)/mCBP (10nm)/DMIC-TRZ: emitter (40 nm)/PO-T2T (20 nm)/ANT-BIZ (30 nm)/Liq (2nm)/AI (100 nm). In the device configuration, 1,4,5,8,9,11-hexaazatriphenylenehexacarbonitrile (HATCN) was served as a hole injection layer; 1,1-bis[(di-4-tolylamino)phenyl]-cyclohexane (TAPC) and (1-(4-(10-([1,1′-biphenyl]-4-yl)anthracen-9-yl)phenyl)-2-ethyl-1H-benzo[d]-imidazole) (ANT-BIZ) were applied as hole- and

electron-transport layers, respectively; 3,3′-di(9H-carbazol-9-yl)-1,1′-biphenyl (mCBP) served as exciton-blocking layers; 1,3-dihydro-1,1-dimethyl-3-(3-(4,6-diphenyl-1,3,5-triazin-2-yl)phenyl)indeno-[2,1-b]carbazole (DMIC-TRZ) was used as the host due to its balanced charge injection and transporting mobilities. The ITO coated glass substrates with a sheet resistance of 15 Ω square^{-1} were consecutively ultrasonicated with acetone/ethanol and dried with nitrogen gas flow, followed by 20 min ultraviolet light-ozone (UVO) treatment in a UV-ozone surface processor (PL16 series, Sen Lights Corporation). Then the sample was transferred to the deposition system. Both 8-hydroxyquinolinolato-lithium (Liq) as electron injection layer and aluminum (Al) as cathode layer were deposited by thermal evaporation at 5×10^{-5} Pa. Additionally, the metal complex layer was deposited at the rates of 0.2-3 Å/s. After the metal complex film deposition, Liq and Al layer were deposited with rates of 0.1 and 3 Å/s, respectively. The emitting area of the device is about 0.09 cm^2. The current 3 density-voltage-luminance (*J*-*V*-*L*), L-EQE curves and electroluminescence spectra were measured using a Keithley 2400 source meter and an absolute EQE measurement system (C9920-12, Hamamatsu Photonics, Japan).

Computational Methods

All geometry optimizations and electronic properties calculations were performed with Gaussian 16 package.[10] The ground-state (S_0) structures were optimized by the density functional theory (DFT)[11] method with the PBE0[12] functional and mixed basis sets in which the SDD[13] basis set and pseudopotential were used for metal atom (Pt) and the DEF2-SVP[14] basis set was used for the C, H, N atoms.[11-12] The excited-state properties were obtained by time-dependent density functional theory (TD-DFT)[15] method at the same level with the S_0 calculations. The spin-orbit couplings (SOCs) were calculated using the PySOC code.[16] No solvent was applied to all calculations, and the results were analyzed further with GaussView.

Synthesis

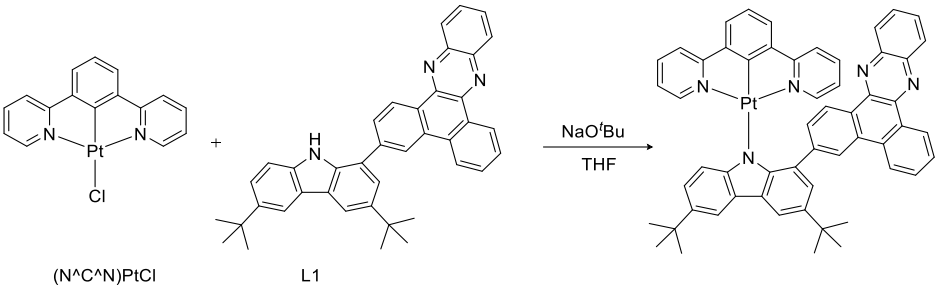

(N^C^N)PtCl L1 Pt-*t*CzDBPZ (Pt1)

Pt-*t*CzDBPZ (Pt1): (N^C^N)PtCl was synthesized according to a reported method.[17] L1 (167 mg, 0.30 mmol) and NaO^{t}Bu (40 mg, 0.40 mmol) were dissolved in dry THF and stirred for 3 h under argon at room temperature, followed by the addition of (N^C^N)PtCl (139 mg, 0.30 mmol). The reaction mixture was stirred for another 12 h. Then, the resulting mixture was filtered through Celite, and the solvent was removed under reduced pressure to afford a red solid. The solid was re-dissolved in dichloromethane, and hexane was added to precipitate the product (224 mg, 76%). ^{1}H NMR (400 MHz, $CDCl_3$) δ (ppm): 9.18 (dd, *J* = 8.0 Hz, *J* = 1.2 Hz, 1H), 8.48 (m, 2H), 8.36 (m, 3H), 8.30 (m, 1H), 8.22 (s, 1H), 7.92 (m, 2H), 7.70 (m, 2H), 7.65 (d, *J* = 8.8 Hz, 2H), 7.54 (m, 2H), 7.46 (d, *J* = 2.4 Hz, 1H), 7.33 (dd, *J* = 8.4 Hz, *J* = 2.0 Hz, 1H), 7.15 (m, 2H), 6.94 (t, *J* = 5.6 Hz, 3H), 6.35 (m, 3H), 5.97 (t, *J* = 7.6 Hz, 1H), 1.60 (s, 9H), 1.52 (s, 9H). ^{13}C NMR (126 MHz, $CDCl_3$) δ 167.45, 166.11, 151.80, 149.42, 148.07, 144.81, 142.43, 142.21, 142.13, 141.69, 138.11, 137.78, 137.58, 132.26, 131.05, 130.16, 129.71, 129.43, 129.37, 129.18, 129.10, 127.87, 126.95, 126.64, 126.08, 125.68, 125.50, 124.90, 124.44, 122.80, 121.86, 121.68, 121.39, 118.73, 115.34, 115.28, 114.16, 34.69, 34.61, 32.47, 32.39. Anal. Calcd for $C_{56}H_{45}PtN_5 \cdot 2CH_2Cl_2$: C, 60.42; N, 6.07; H, 4.28. Found: C, 60.76; N, 5.94; H, 4.17. HRMS-ESI: m/z calculated for $C_{56}H_{46}PtN_5^+$ $[M+H]^+$ 983.3401, found 983.3402.

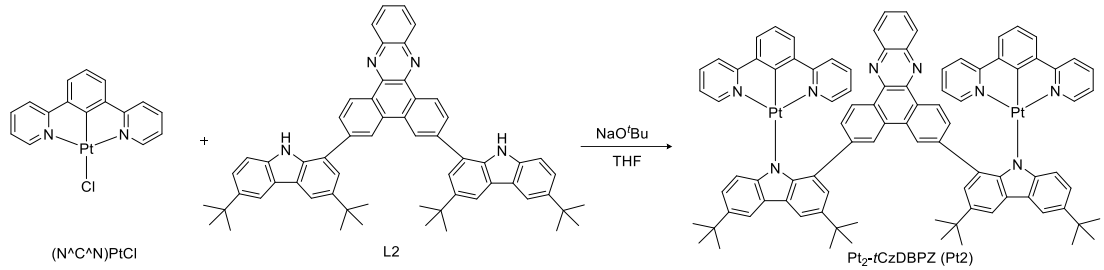

Pt$_2$-*t*CzDBPZ (Pt2): The complex was made from (N^C^N)PtCl (139 mg, 0.30 mmol), L2 (250 mg, 0.30 mmol), and NaO^{t}Bu (40 mg, 0.40 mmol) as a red solid (187 mg, 70%). ^{1}H NMR (400 MHz, $CDCl_3$) δ (ppm): 8.26 (m, 6H), 8.20 (d, *J* = 8.1 Hz, 2H), 7.95 (dd, *J* = 6.4, *J* = 3.4 Hz, 2H), 7.81 (m, 4H), 7.61 (m, 2H), 7.52 (d, *J* = 8.6 Hz, 4H), 7.33 (m, 4H), 7.25 (dd, *J* = 8.6, *J* = 2.0 Hz, 2H), 7.19 (d, *J* = 2.0 Hz, 2H), 6.99 (d, *J* = 8.1 Hz, 2H), 6.78 (m, 6H), 6.28 (m, 4H), 5.69 (t, *J* = 7.6 Hz, 2H), 1.62 (s, 18H), 1.46 (s, 18H). ^{13}C NMR (126 MHz, $CDCl_3$) δ 165.79, 149.33, 147.84, 144.12, 142.16, 141.66, 137.68, 136.91, 131.65, 128.89, 128.87, 128.77, 128.09, 126.92, 125.90, 125.58, 124.29, 123.89, 122.70, 121.55, 121.03, 120.57, 115.21, 115.13, 113.99, 34.69, 34.54, 32.61, 32.32. Anal. Calcd for $C_{92}H_{78}Pt_2N_8$: C, 65.55; N, 6.65; H, 4.66. Found: C, 65.83; N, 6.77; H, 4.50. HRMS-ESI: m/z calculated for $C_{92}H_{79}Pt_2N_8^+$ $[M+H]^+$ 1685.5723, found 1685.5681.

Table S1. X-ray crystallographic data of the single crystals of **Pt1** and **Pt2**.

	Pt1 (CH_2Cl_2)	**Pt2 (CH_2Cl_2)**
CCDC	2205684	2205685
Temperature/K	298	100
Formula	$C_{56.7}H_{47.8}Cl_{1.4}N_5Pt$	$C_{92}H_{78}N_8Pt_2$, 2.5(CH_2Cl_2)
Formula weight	1044.42	1898.11
Crystal system	orthorhombic	triclinic
Space group	Pbcn	P-1
a (Å)	23.010(3)	10.4337(9)
b (Å)	11.9854(16)	14.7984(12)
c (Å)	35.310(5)	26.389(2)
α (°)	90	80.853(3)
β (°)	90	86.481(4)
γ (°)	90	87.970(3)
V ($Å^3$)	9738(2)	4013.8(6)
Z Value	8	2
ρ_{calc} / $g \cdot cm^{-3}$	1.424	1.571
μ/mm^{-1}	6.421	8.368
F (000)	4199.0	1894.0
Crystal size	0.22 × 0.16 × 0.02	0.41 × 0.12 × 0.07
2Theta range (°)	5.006-136.904	6.052-137.924
GOF on F^2	1.048	1.029
R_1/wR_2 [I>=2σ (I)]	0.0733-0.2039	0.0594-0.1686

Table S2. Selected bond lengths (Å), and bond angles (degree) for **Pt1** and **Pt2**.

	Pt1	**Pt2**
Bond length (Å)		
Pt-C_{42}/Pt1-C_{79}, Pt2-C_{33}	1.897	1.907, 1.923
Pt-N_1/Pt1-N_1, Pt2-N_4	2.120	2.154, 2.144
C_{42}-N_1 (Pt1)/C_{79}-N_1, C_{33}-N_4 (Pt2)	4.017	4.061, 4.067
Bond angles (degree)		
C_{42}-Pt-N_1/C_{79}-Pt1-N_1, C_{33}-Pt2-N_4 (Pt2)	175.6	175.8, 176.2
Bond angles around N_{tCz}		
C_4-N_1-C_1/ C_4-N_1-C_1, C_{30}-N_4-C_{47} (Pt2)	104.2	105.9, 107.4
C_4-N_1-Pt/ C_4-N_1-Pt1, C_{30}-N_4-Pt2 (Pt2)	127.2	125.1, 125.8
C_1-N_1-Pt/ C_1-N_1-Pt1, C_{47}-N_4-Pt2 (Pt2)	128.0	129.0, 123.2
ΣN_{Cz}	359.4	360, 356.4

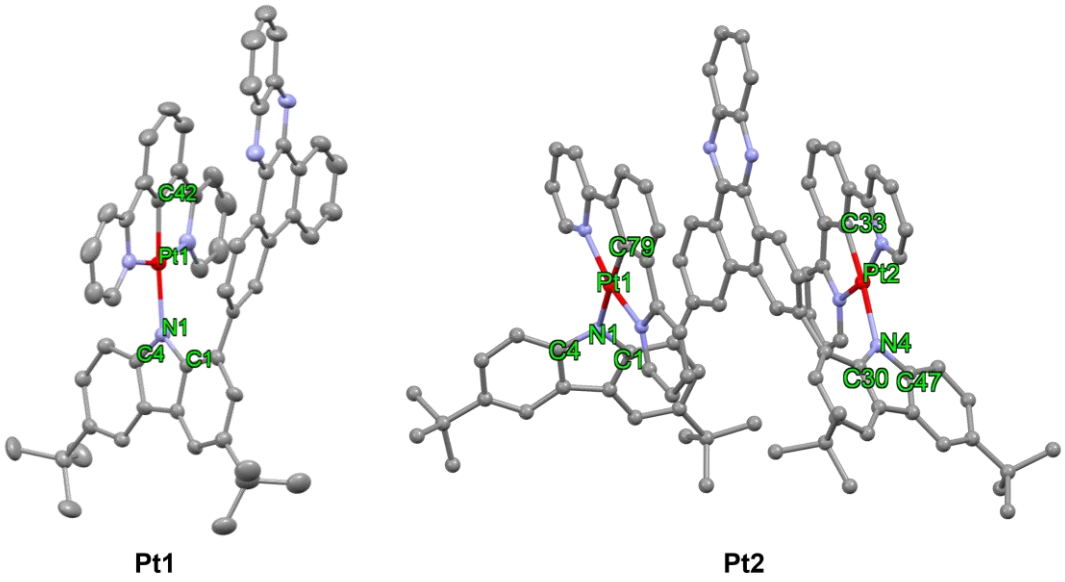

Figure S1. The perspective view of X-ray crystal structures of **Pt1** and **Pt2** with labelled atoms.

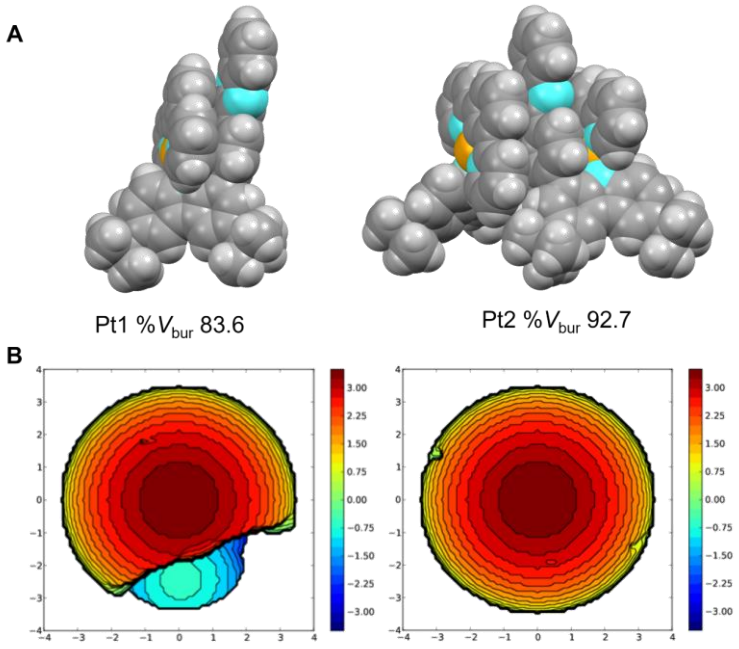

Figure S2. A) The space-filling diagrams and B) buried volume %V_{bur} around the Pt atom in **Pt1** and **Pt2**.

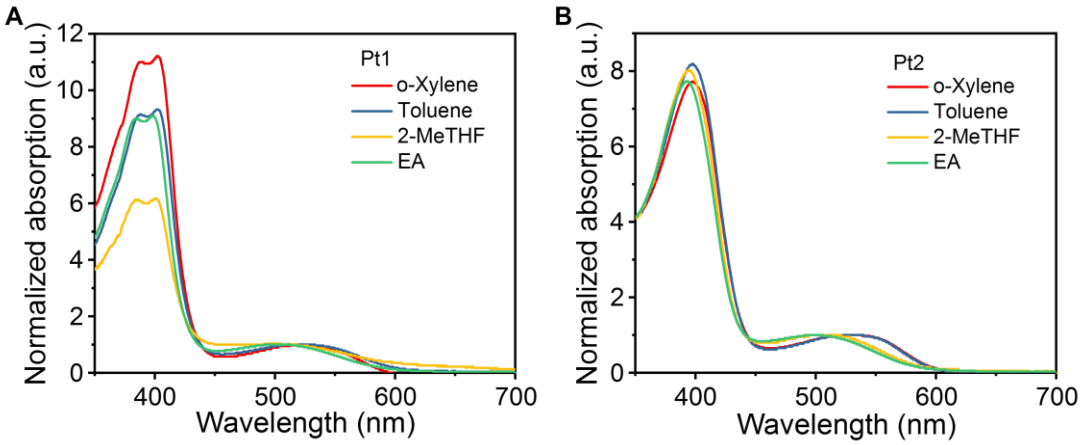

Figure S3. The normalized absorption spectra of A) **Pt1** and B) **Pt2** in different solvents at 298 K (1×10^{-5} M).

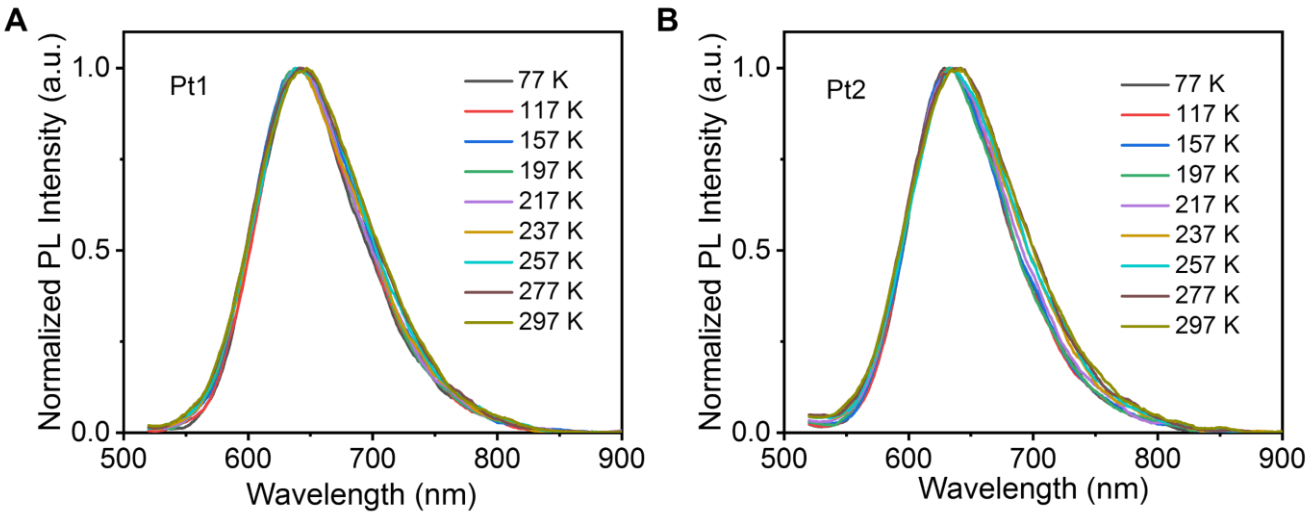

Figure S4. Temperature dependent steady-state photoluminescence of A) **Pt1** and B) **Pt2** doped in 5wt% PMMA films with excitation at 485 nm.

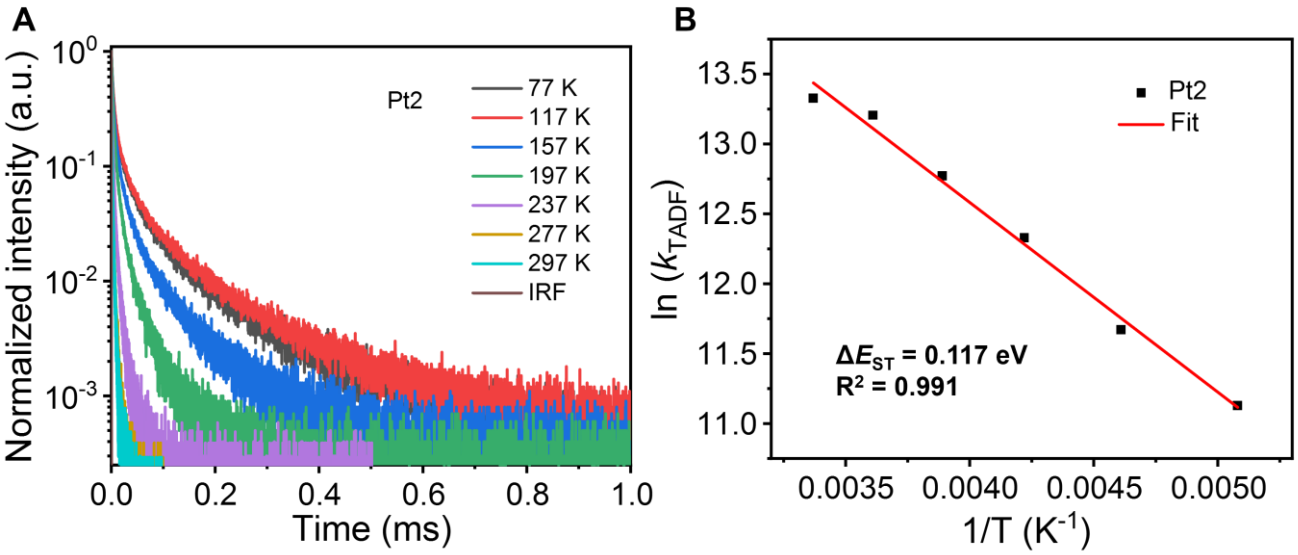

Figure S5. A) Variable temperature photoluminescence decay characteristics of **Pt2** and B) Arrhenius fit of the kinetic data of **Pt2** in 5wt% PMMA film (Arrhenius analysis taking from Equation S1).

Table S3. Temperature dependent photophysical properties of **Pt1** in 5wt% PMMA film.

T[a] (K)	τ[b] (μs)	τ_1 (μs)	τ_2 (μs)	τ_3 (μs)	$k_{r,TADF}$[c] (10^5 s^{-1})
157	37.1	4.77 (28%)	24.5 (50%)	107 (22%)	0.27
177	23.0	3.74 (33%)	16.7 (49%)	75.6 (18%)	0.43
197	12.4	2.88 (40%)	10.9 (47%)	47.2 (13%)	0.81
217	6.64	3.01 (70%)	15.1 (30%)	-	1.51
237	4.08	2.10 (72%)	9.16 (28%)	-	2.45
257	2.93	1.66 (74%)	6.54 (26%)	-	3.41
277	1.91	1.19 (75%)	4.07 (25%)	-	5.24
297	1.51	1.00 (75%)	3.07 (25%)	-	6.62

[a] Measured in PMMA film at different temperature. [b] Calculated from the weighted average of the two or three contributions. [c] $k_{r,TADF} = 1/\tau$.

Table S4. Temperature dependent photophysical properties of **Pt2** in 5wt% PMMA film.

T[a] (K)	τ[b] (μs)	τ_1 (μs)	τ_2 (μs)	τ_3 (μs)	$k_{r,TADF}$[c] (10^5 s^{-1})
197	14.7	2.76 (39%)	11.8 (45%)	52.2 (16%)	0.68
217	8.57	2.07 (41%)	7.72 (46%)	32.1 (13%)	1.17
237	4.42	1.30 (40%)	4.15 (48%)	15.9 (12%)	2.26
257	2.84	1.42 (70%)	6.14 (30%)	-	3.52
277	1.84	0.95 (68%)	3.72 (32%)	-	5.43
297	1.63	0.90 (69%)	3.26 (31%)	-	6.13

[a] Measured in PMMA film at different temperature. [b] Calculated from the weighted average of the two or three contributions. [c] $k_{r,TADF} = 1/\tau$.

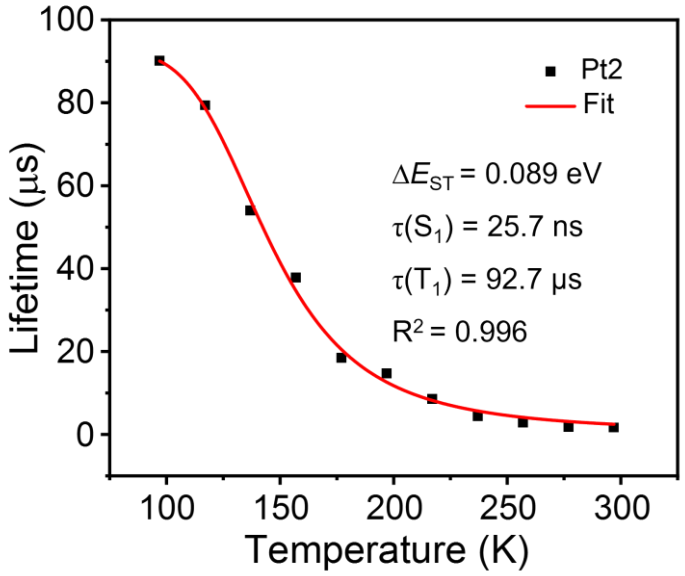

Figure S6. The Boltzmann-type equation fitting of the emission lifetimes of **Pt2** in PMMA film at various temperatures (Boltzmann Equation S2). The decay plots of their emission lifetime against temperature showed an excellent fit (R^2 = 0.996). The $\Delta E_{(S1\text{-}T1)}$ is 89 meV, and the value is close to the value (117 meV for **Pt2**) extracted from Arrhenius plots (Arrhenius Equation S1).

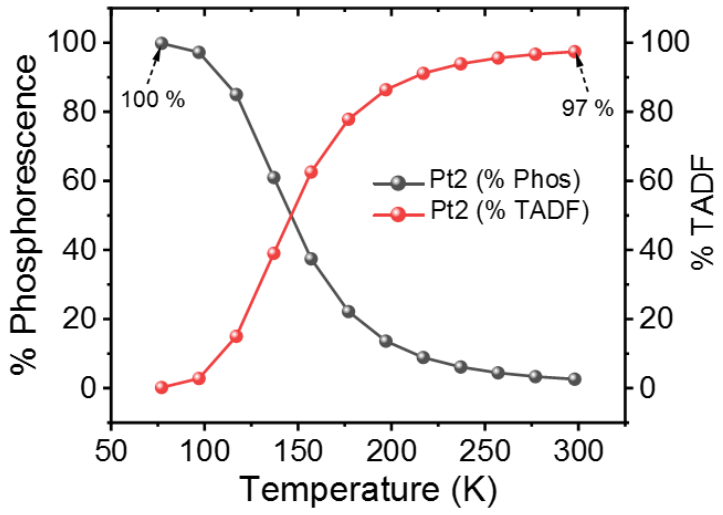

Figure S7. TADF vs. T_1 phosphorescence of **Pt2** as a function of temperature. The data was used to generate the plots of % TADF and % T_1 Phosphorescence shown in this picture (Taking from Equation S3). Note that above 298 K **Pt2** give > 97% TADF emission.

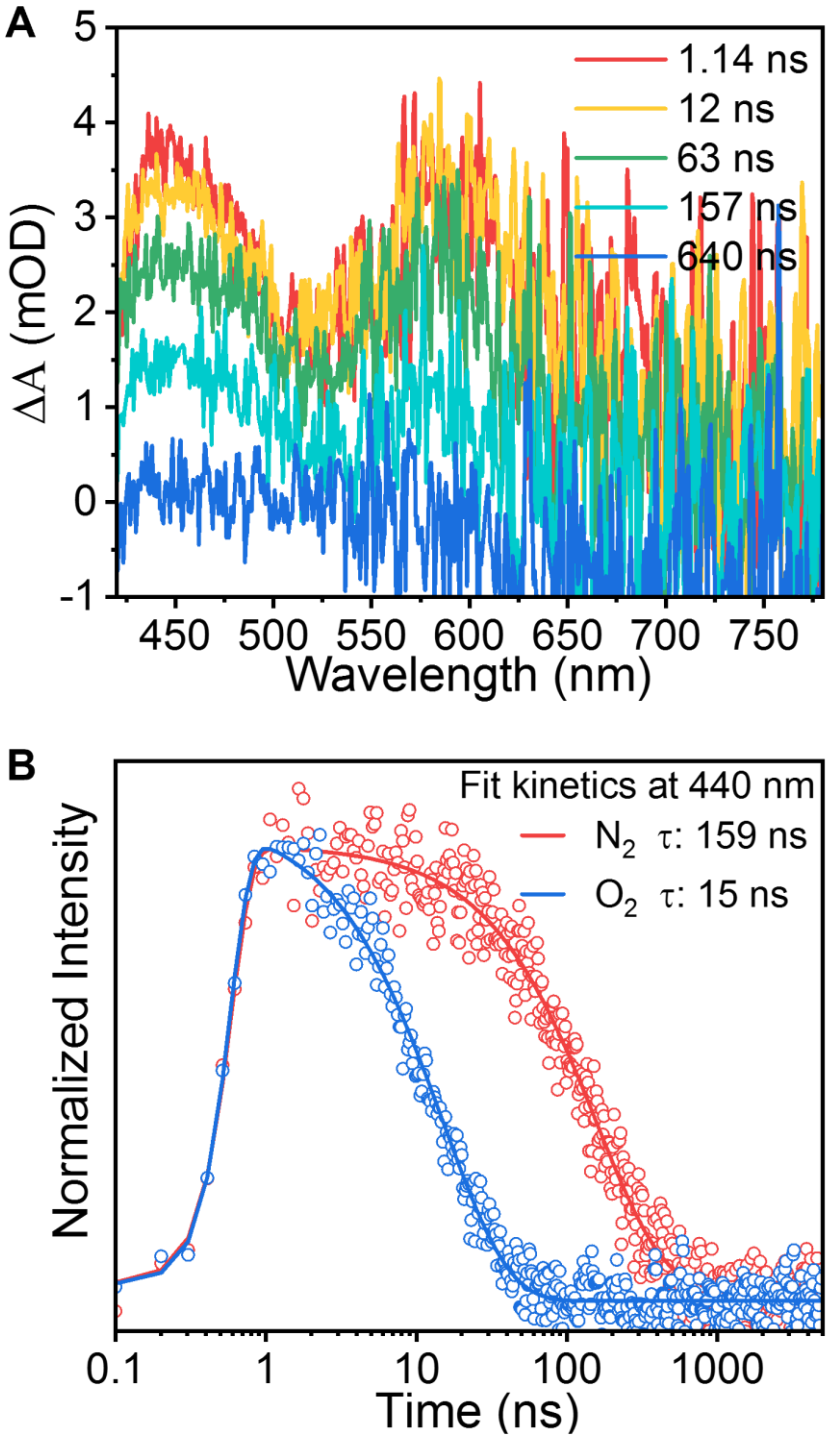

Figure S8. A) Ns-TA evolution spectra of **Pt1** under nitrogen, and B) kinetics at 440 nm of **Pt1** (concentration = 0.25 mM, λ_{ex} = 400 nm).

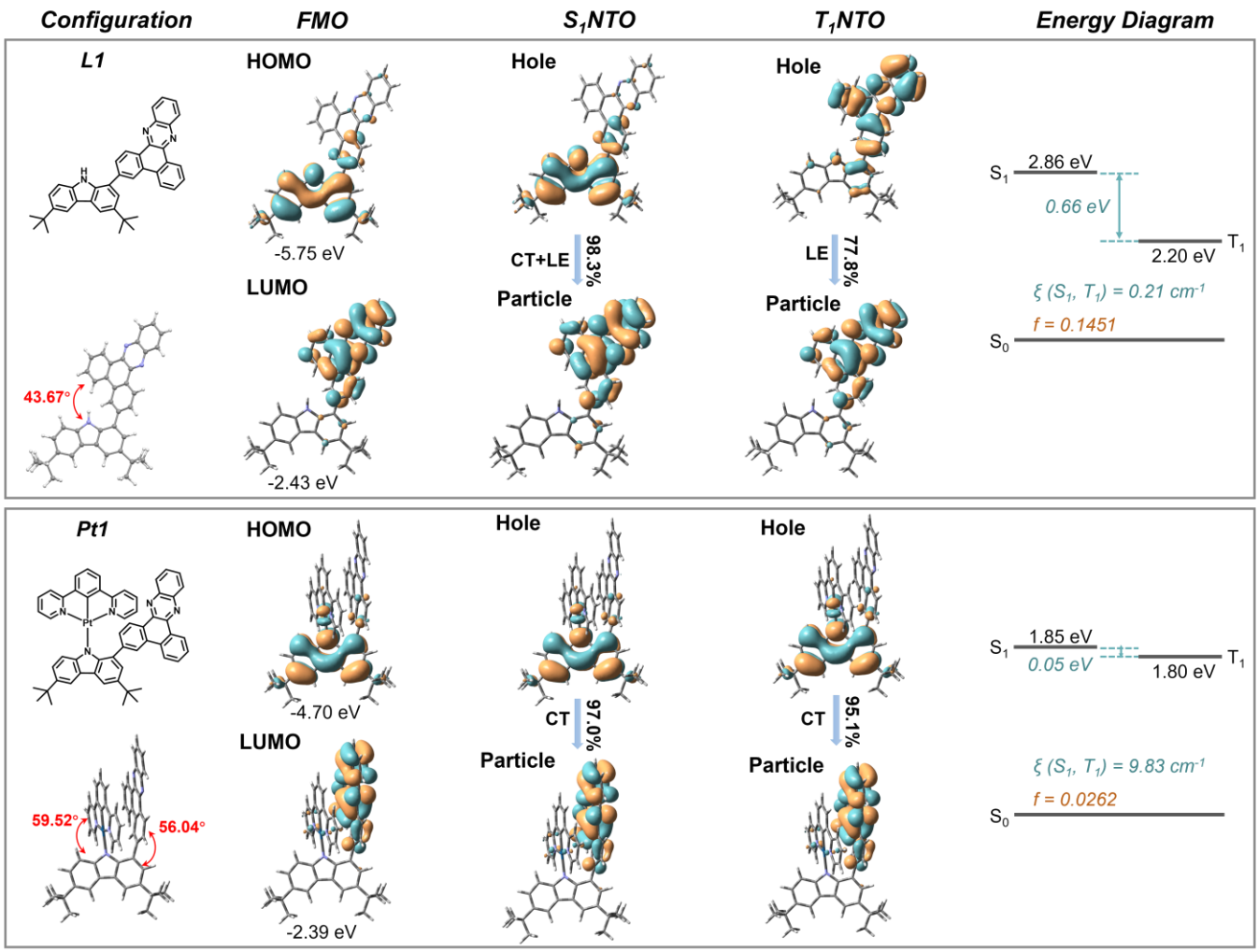

Figure S9. The optimized ground-state geometries, frontier molecular orbitals, the natural transition orbitals (NTOs) analyses and the excited states energy levels of L1 and **Pt1**.

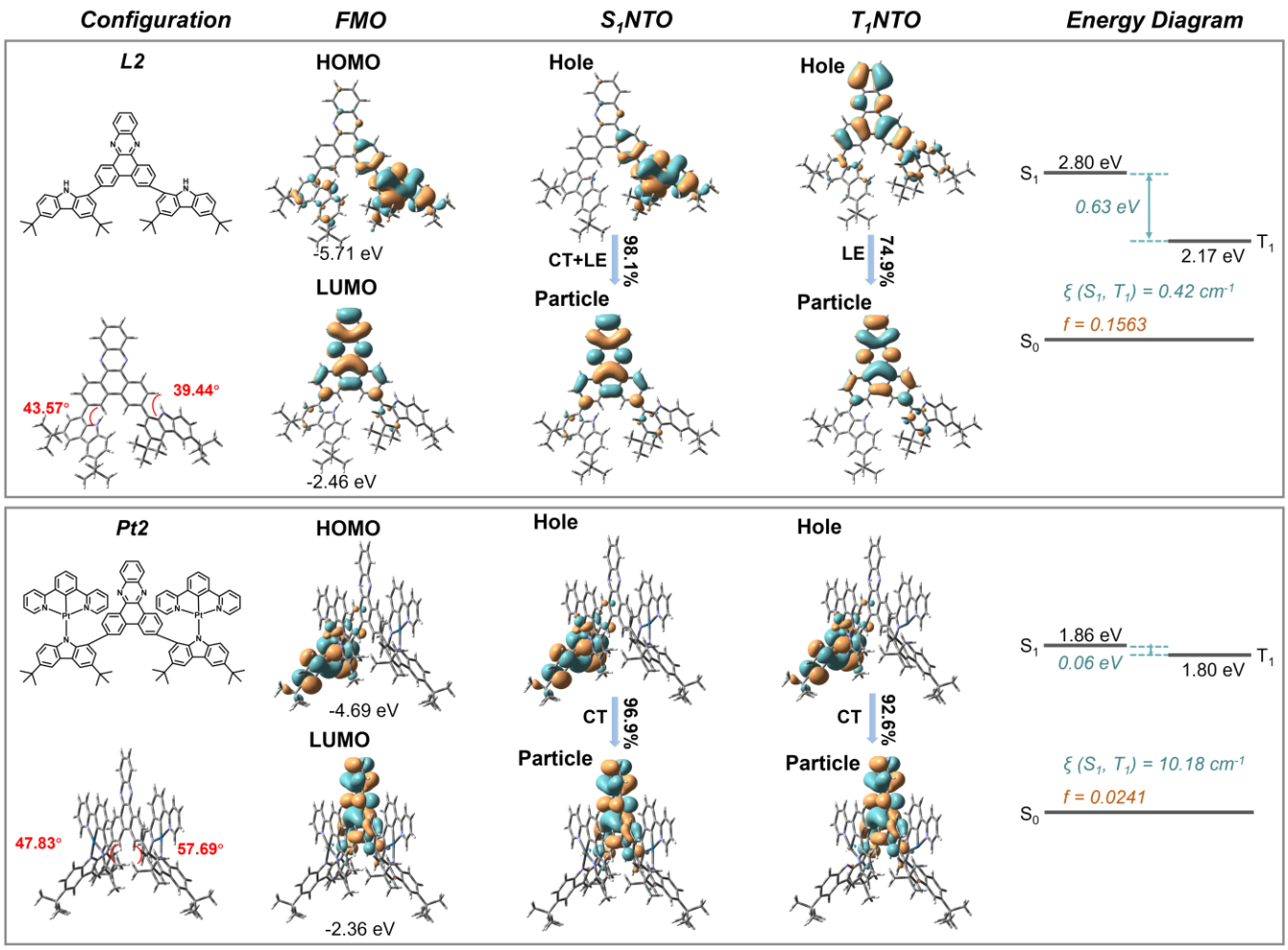

Figure S10. The optimized ground-state geometries, frontier molecular orbitals, the natural transition orbitals (NTOs) analyses and the excited states energy levels of L2 and **Pt2**.

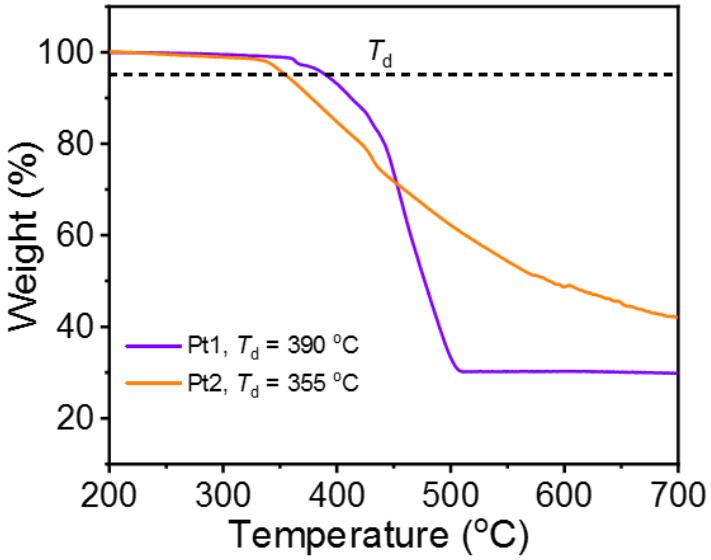

Figure S11. The thermogravimetric analysis (TGA) curves of **Pt1** and **Pt2** under N_2 atmosphere.

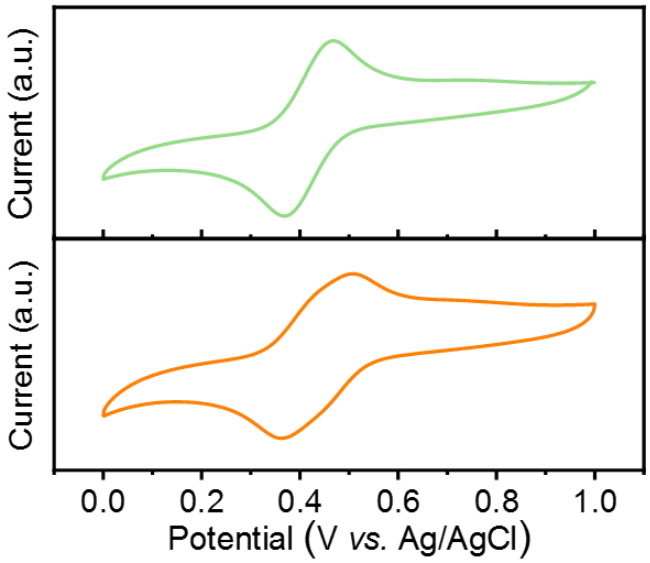

Figure S12. Cyclic voltammograms (CV) of **Pt1** (green) and **Pt2** (orange) in CH_2Cl_2 at 298 K.

Table S5. Electrochemical data and estimated FMO energy levels of **Pt1** and **Pt2** in CH_2Cl_2.

complex	E_{pa}[a] (V)	E_{pc}[a] (V)	$E_{1/2}$(ox)[a] (V)	E_g[b] (eV)	HOMO[c] (eV)	LUMO[d] (eV)
Pt1	0.47	0.37	0.42	2.18	-4.73	-2.55
Pt2	0.45, 0.50	0.43, 0.36	0.41, 0.47	2.14	-4.72, -4.78	-2.58, -2.64

[a] Measured in dichloromethane. $E_{1/2}(ox) = (E_{pa} + E_{pc})/2$. [b] Estimated from absorption onset, $E_g = 1240/\lambda$. [c] The HOMOs estimated by $E_{HOMO} = -e[E_{1/2}(ox) - E_{1/2}(Fc^+/Fc)] - 4.8$ eV. $E_{1/2}(Fc^+/Fc) = 0.49$ V. [d] $E_{LUMO} = E_{HOMO} + E_g$.

Table S6. The device performance of representative red TADF OLEDs in the literature (λ_{EL} > 600 nm, EQE_{max} > 20%).

Emitter	λ_{em} [nm]	EQE_{max} [%]	CE_{max} [cd A^{-1}]	PE_{max} [lm W^{-1}]	CIE (x, y)	Reference
Pt1 (1wt%)	**610**	**35.6**	**61.2**	**60.7**	**(0.58, 0.42)**	**This work**
Pt1 (3 wt%)	**615**	**32.1**	**45.9**	**43.5**	**(0.60, 0.40)**	**This work**
DPXZ-BPPZ	612	20.1	30.2	30.9	(0.60, 0.40)	*Adv. Sci*. **2018**, *5*, 1800436
Da-CNBQx	617	20.0	28.9	32.4	(0.59, 0.41)	*Adv. Opt. Mater*. **2018**, *6*, 1701147
BPPZ-PXZ	604	25.2	37.0	41.0	(0.58, 0.42)	*Angew. Chem. Int. Ed.* **2019**, *58*, 14660
mBPPZ-PXZ	624	21.7	25.0	21.0	(0.62, 0.38)	*Angew. Chem. Int. Ed.* **2019**, *58*, 14660
TPA-PZCN	648	28.1	20.0	26.3	(0.66, 0.34)	*Adv. Mater*. **2019**, *31*, 1902368
ANQDC-MeFAC	614	26.3	41.4	46.5	(0.60, 0.40)	*Adv. Funct. Mater*. **2020**, *30*, 1908839
ANQDC-DMAC	615	27.5	47.6	53.1	(0.58, 0.41)	*Adv. Funct. Mater*. **2020**, *30*, 1908839
BBCz-R	616	22.0	–	–	(0.67, 0.33)	*J. Am. Chem. Soc*. **2020**, *142*, 19468
T-DA-2	640	26.3	24.4	22.5	(0.62, 0.37)	*Adv. Funct. Mater*. **2020**, *30*, 2002681
FBPCNAc	606	20.8	38.3	37.8	(0.58, 0.42)	*ACS Appl. Mater. Interfaces* **2020**, *12*, 18730
DCPPr-α-NDPA	606	31.5	59.6	58.4	(0.58, 0.42)	*Angew. Chem. Int. Ed*. **2021**, *60*, 23635
DCPPr-TPA	616	27.5	47.5	46.6	(0.59, 0.41)	*Angew. Chem. Int. Ed*. **2021**, *60*, 23635
oDTBPZ-DPXZ	604	20.1	38.1	29.2	(0.59, 0.41)	*Angew. Chem. Int. Ed*. **2021**, *60*, 2478
PT-TPA	632	29.7	30.0	38.5	(0.64, 0.35)	*Mater. Horiz*. **2021**, *8*, 1297

BNO1	610	35.6	59.4	66.7	(0.64, 0.34)	*Adv. Mater*. **2022**, *34*, e2201442
BNO2	618	34.4	46.5	52.2	(0.65, 0.35)	*Adv. Mater*. **2022**, *34*, e2201442
BNO3	625	36.1	43.4	48.7	(0.66, 0.34)	*Adv. Mater*. **2022**, *34*, e2201442
BN-R	617	22.0	30.2	31.2	(0.65, 0.34)	*Angew. Chem. Int. Ed*. **2023**, *62*, e202216473
CzIDBNO	643	32.5	20.2	24.1	(0.70, 0.30)	*Sci. Adv*. **2023**, *9*, eadh8296
IDIDBNO	671	27.2	8.4	8.8	(0.70, 0.30)	*Sci. Adv*. **2023**, *9*, eadh8296
Pd1	640	30.1	29.6	27.5	(0.63, 0.37)	*Sci. Adv*. **2023**, *9*, eadh0198

Table S7. The device performance of representative red phosphorescence doped OLEDs of Pt(II) and Ir(III) complexes in the literature (λ_{EL} > 600 nm, EQE_{max} > 20%).

Emitter	λ_{em} [nm]	EQE_{max} [%]	CE_{max} [cd A^{-1}]	PE_{max} [lm W^{-1}]	CIE (x, y)	Reference
Pt1 (1wt%)	**610**	**35.6**	**61.2**	**60.7**	**(0.58, 0.42)**	**This work**
Pt1 (3 wt%)	**615**	**32.1**	**45.9**	**43.5**	**(0.60, 0.40)**	**This work**
PtN3N-ptb	606	21.5	–	–	(0.58, 0.42)	*ACS Appl. Mater. Interfaces* **2015**, *7*, 16240
1	639	23.3	24.4	26.8	(0.62, 0.38)	*Angew. Chem. Int. Ed*. **2022**, *61*, e202113718
2	625	21.0	29.0	26.5	(0.60, 0.39)	*Angew. Chem. Int. Ed*. **2022**, *61*, e202113718
Pt(TPA)(py)(iq)	609	31.8	50.5	56.7	(0.62, 0.38)	*Adv. Mater.* **2023**, *35*, 2303066
Pt(TPA)(py)(*δ*-Cbl)	643	26.3	14.0	15.7	(0.68, 0.32)	*Adv. Mater.* **2023**, *35*, 2303066
Pt(TPA)(iq)(*δ*-Cbl)	638	30.8	23.8	26.7	(0.67, 0.33)	*Adv. Mater.* **2023**, *35*, 2303066
Ir(pimb)(L3)	643	27.4	36.9	36.2	(0.63, 0.38)	*Adv. Mater*. **2016,** *28*, 2795.
PMD-Ir-3	608	27.6	46.1	55.7	(0.63, 0.36)	*Adv. Optical Mater*. **2018**, *6*, 1800108
PMD-Ir-4	608	23.1	37.4	41.9	(0.63, 0.36)	*Adv. Optical Mater.* **2018**, *6*, 1800108
Ir(4tfmpq)2mND	628	30.1	25.6	18.5	(0.67, 0.33)	*ACS Appl. Mater. Interfaces* **2019**, *11*, 20192
Ir(4tfmpq)2mmND	628	31.5	25.2	19.3	(0.67, 0.33)	*ACS Appl. Mater. Interfaces* **2019**, *11*, 20192

Ir(4tfmpq)2mpND	620	27.7	27.0	22.8	(0.66, 0.34)	*ACS Appl. Mater. Interfaces* **2019**, *11*, 20192
1F-Ir	622	26.8	23.8	30.5	(0.66, 0.33)	*Chem. Eur. J.* **2020**, *26*, 4410
2F-Ir	612	24.3	24.5	32.1	(0.64, 0.35)	*Chem. Eur. J.* **2020**, *26*, 4410
^{n}BuIr(dbpz)CN	628	20.7	17.1	21.2	(0.68, 0.32)	*Small* **2023**, 2307500

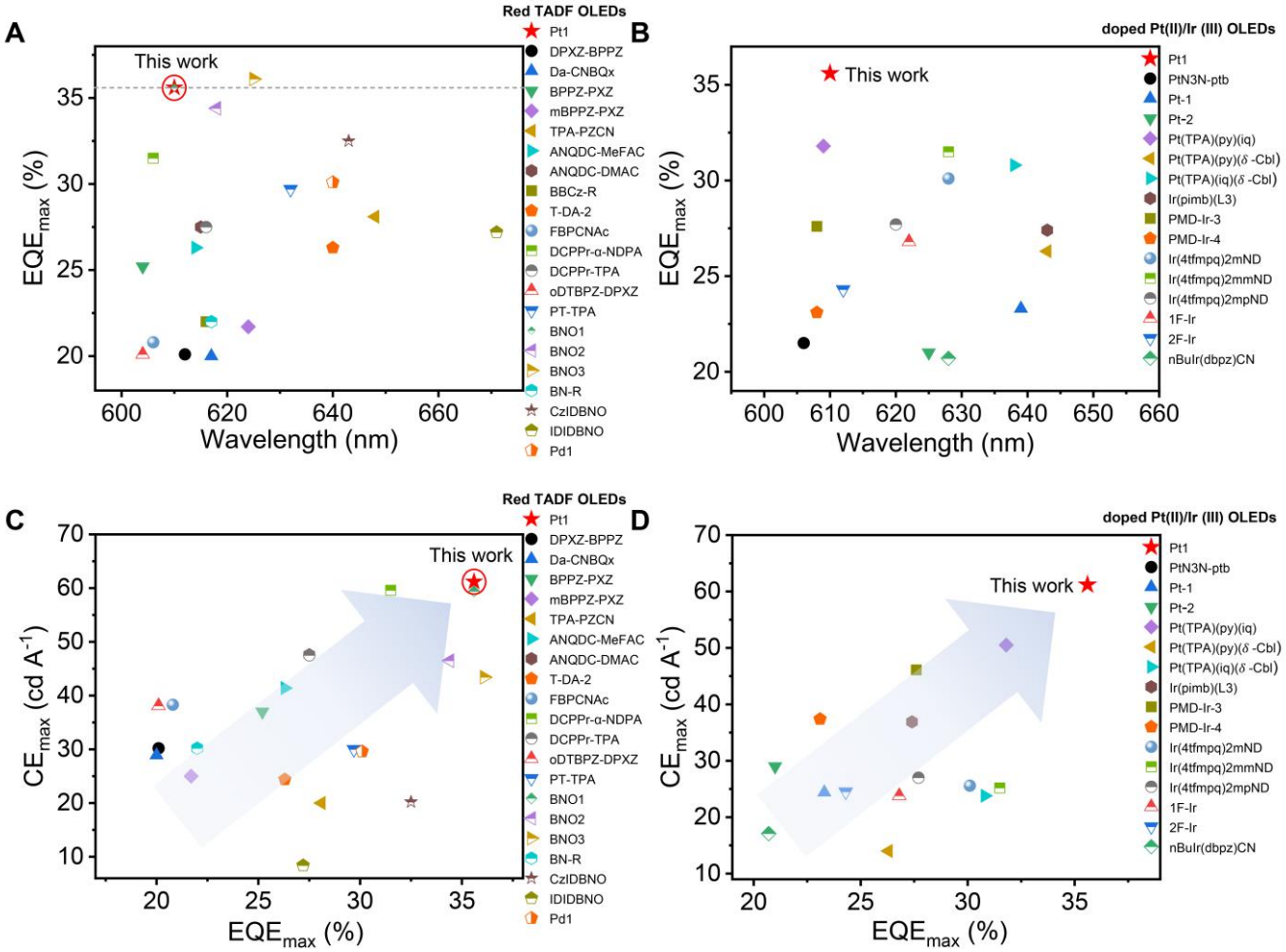

Figure S13. The maximum EQE versus EL peak wavelength of some representative high-efficiency A) TADF and B) phosphorescence OLEDs in the literature. C) D) maximum CE values versus maximum EQE of representative red OLEDs.

NMR Spectra

$^{1}H/^{13}C$ NMR spectra

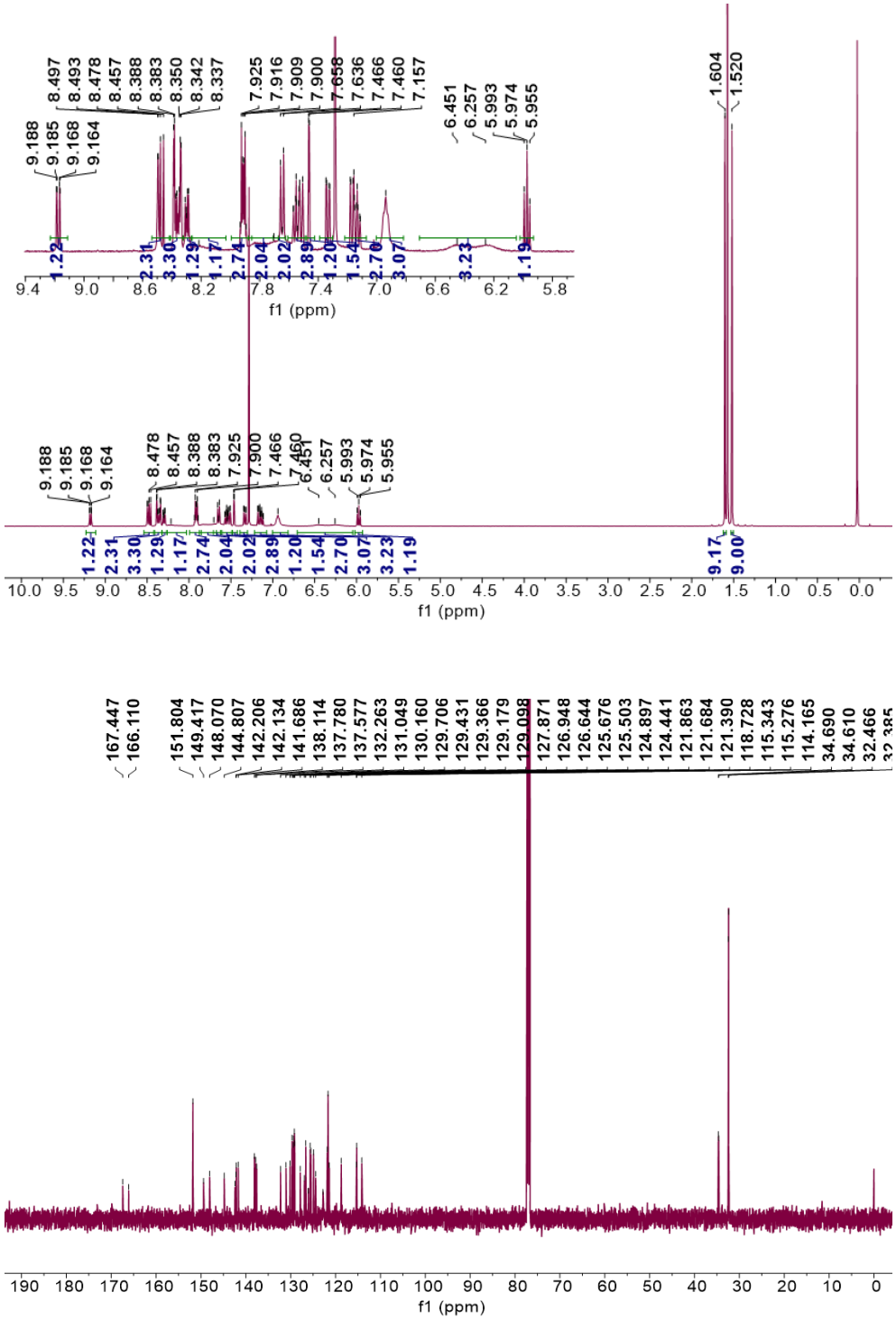

Figure S14. NMR spectra for **Pt1**. ^{1}H NMR (400 MHz, $CDCl_3$); ^{13}C NMR (126 MHz, $CDCl_3$).

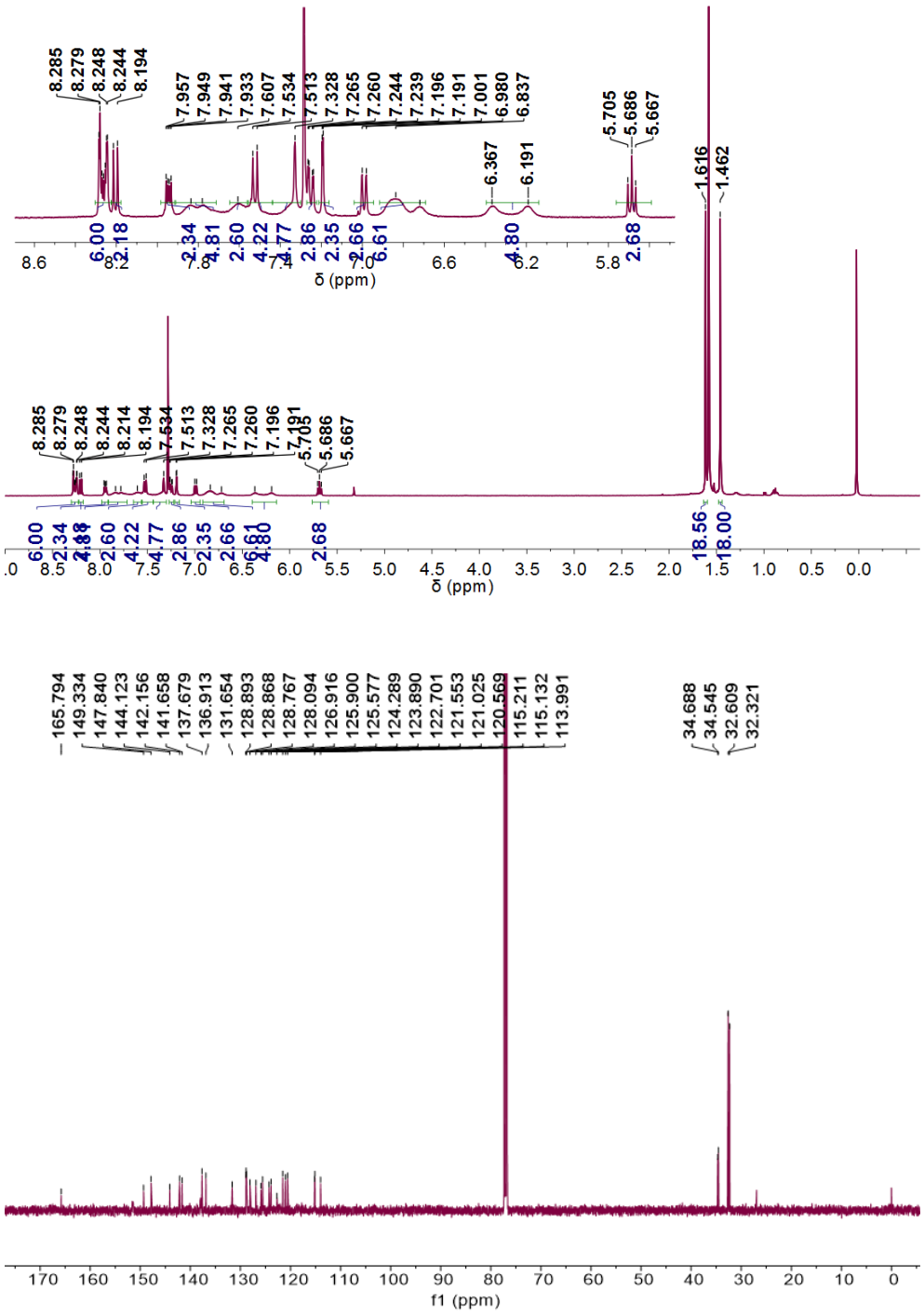

Figure S15. NMR spectra for **Pt2**. ^{1}H NMR (400 MHz, $CDCl_3$); ^{13}C NMR (126 MHz, $CDCl_3$).

References

[1] C. Jiang, J. Miao, D. Zhang, Z. Wen, C. Yang, K. Li, *Research*, **2022**, *2022*, 9892802.

[2] J.-G. Yang, X. Feng, G. Xie, N. Li, J. Li, X.-F. Song, M.-D. Li, J. Zhang, X. Chang, K. Li, *Sci. China Chem*. 2024. DOI: 10.1007/s11426-024-2026-2.

[3] R. Hamze, S. Shi, S. C. Kapper, D. S. Muthiah Ravinson, L. Estergreen, M. C. Jung, A. C. Tadle, R. Haiges, P. I. Djurovich, J. L. Peltier, R. Jazzar, G. Bertrand, S. E. Bradforth, M. E. Thompson, *J. Am. Chem. Soc*. **2019**, *141*, 8616-8626.

[4] Y. Tsuchiya, S. Diesing, F. Bencheikh, Y. Wada, P. L. dos Santos, H. Kaji, E. Zysman-Colman, I. D. W. Samuel, C. Adachi, *J. Phys. Chem. A* **2021**, 125, 8074–8089.

[5] H. Yersin, A. F. Rausch, R. Czerwieniec, T. Hofbeck, T. Fischer, *Coord. Chem. Rev*. **2011**, *255,* 2622-2652.

[6] R. Czerwieniec, M. J. Leitl, H. H. H. Homeier, H. Yersin, *Coord. Chem. Rev*. **2016**, *325*, 2-28.

[7] O. V. Dolomanov, L. J. Bourhis, R. J. Gildea, J. A. K. Howard, H. Puschmann, *J. Appl. Cryst*. **2009**, *42*, 339-341.

[8] G. M. Sheldrick, *Acta. Cryst*. **2015**, *A71*, 3-8.

[9] G. M. Sheldrick, *Acta. Cryst.* **2015**, *C71*, 3-8.

[10] M. J. Frisch, G. W. Trucks, H. B. Schlegel, G. E. Scuseria, M. A. Robb, J. R. Cheeseman, G. Scalmani, V. Barone, G. A. Petersson, H. Nakatsuji, X. Li, M. Caricato, A. V. Marenich, J. Bloino, B. G. Janesko, R. Gomperts, B. Mennucci, H. P. Hratchian, J. V. Ortiz, A. F. Izmaylov, J. L. Sonnenberg, D. Williams-Young, F. Ding, F. Lipparini, F. Egidi, J. Goings, B. Peng, A. Petrone, T. Henderson, D. Ranasinghe, V. G. Zakrzewski, J. Gao, N. Rega, G. Zheng, W. Liang, M. Hada, M. Ehara, K. Toyota, R. Fukuda, J. Hasegawa, M. Ishida, T. Nakajima, Y. Honda, O. Kitao, H. Nakai, T. Vreven, K. Throssell, J. A. Montgomery, Jr., J. E. Peralta, F. Ogliaro, M. J. Bearpark, J. J. Heyd, E. N. Brothers, K. N. Kudin, V. N. Staroverov,

T. A. Keith, R. Kobayashi, J. Normand, K. Raghavachari, A. P. Rendell, J. C. Burant, S. S. Iyengar, J. Tomasi, M. Cossi, J. M. Millam, M. Klene, C. Adamo, R. Cammi, J. W. Ochterski, R. L. Martin, K. Morokuma, O. Farkas, J. B. Foresman, and D. J. Fox, Gaussian 16 Revision C.01, Gaussian, Inc., Wallingford CT, 2019.

[11] R. Parr, W. Yang, Oxford Univ: **1989**.

[12] C. Adamo, V. Barone, *J. Chem. Phys.* **1999**, *110*, 6158-6169.

[13] D. Andrae, U. Häussermann, M. Dolg, H. Stoll, H. Preuss, *Theoret. Chim. Acta.* **1990**, *77*, 123-141.

[14] F. Weigend, R. Ahlrichs, *Phys. Chem. Chem. Phys.* **2005**, *7*, 3297-3305.

[15] M. Marques, A. Rubio, E. K. Gross, K. Burke, F. Nogueira, C. A. Ullrich, Springer Science & Business Media: 2**006**; Vol. 706.

[16] X. Gao, S. Bai, D. Fazzi, T. Niehaus, M. Barbatti, W. Thiel, *J. Chem. Theory Comput*. **2017**, *13*, 515–524.

[17] D.J. Ca´rdenas, A.M. Echavarren, *Organometallics* **1999**, *18*, 3337-3341.